Journal of Solid State Chemistry **143,** 202–209 (1999)
Article ID jssc.1998.8077, available online at http://www.idealibrary.com on IDEAL®

Structural Study of $La_{0.8}Sr_{0.2}Ga_{0.85}Mg_{0.15}O_{2.825}$

Aniceta Skowron, Peng-nian Huang, and Anthony Petric[1]

Department of Materials Science and Engineering, McMaster University, Hamilton, Ontario, L8S 4L7 Canada

Received April 8, 1998; in revised form October 19, 1998; accepted October 20, 1998

The structure of $La_{0.8}Sr_{0.2}Ga_{0.85}Mg_{0.15}O_{2.825}$ was studied by powder neutron diffraction and transmission electron microscopy. Neutron powder diffraction revealed cubic symmetry but electron diffraction and imaging showed the presence of local superstructures with symmetry lower than the average cubic. The thermal stability of the superstructures was investigated using high-temperature electron diffraction. One of the superstructures was related to ordering of the oxygen vacancies into planes normal to $\langle 100\rangle_c$. Increasing the temperature destroys this planar ordering and eliminates the associated streaking on the electron diffraction pattern. The temperature of the disappearance of the streaking correlates with the change in conduction activation energy above 500°C. After rapid cooling in the electron microscope, the ordering is fully restored to its original form, consistent with the hypothesis that the superstructure is formed by ordering of a very mobile ion, such as oxygen, in $La_{0.8}Sr_{0.2}Ga_{0.85}Mg_{0.15}O_{2.825}$.

Key Words: **lanthanum gallate; oxygen electrolyte; perovskite.**

1. INTRODUCTION

In $La_{0.8}Sr_{0.2}Ga_{0.85}Mg_{0.15}O_{2.825}$ and other oxygen-deficient oxides, oxygen transport occurs by way of oxygen vacancies, which implies that the transport properties critically depend on the kinetics of oxygen motion and on trapping processes. The random distribution of freely moving vacancies, formed by doping or reduction, is the optimal but never realized scenario. Because some of the oxygen vacancies are always trapped near dopant ions, the number of vacancies available for oxygen transport in the material is smaller than that deduced from the stoichiometry. However, if the vacancies order in some cooperative manner, they become trapped even more effectively than in the case of random distribution of dopant ions. Even if the regions over which the cooperative vacancy ordering occurs are small, they still have profound effects on the kinetics of the oxygen motion, because of their large trapping energy and the localized character of the oxygen diffusion. Recent investigations into heavily doped perovskites show that macroscopic cubic symmetry does not necessarily lead to a random distribution of oxygen vacancies (1, 2) and that regions with lower local symmetry, which might be associated with ordering of vacancies, do exist in these materials. The discovery of high conductivity in doped, perovskite-type lanthanum gallate (3, 4) has prompted us to study the local structures in $La_{0.8}Sr_{0.2}Ga_{0.85}Mg_{0.15}O_{2.82}$. Using electron diffraction we have obtained evidence for small domains with local symmetry lower than the average cubic symmetry. We have also identified regions wherein we postulate the planar ordering of oxygen vacancies which dissociate with increasing temperature and reconstitute on cooling.

$LaGaO_3$ adopts the orthorhombic perovskite structure (*Pnma*), isostructural with $GdFe_3O$ but transforms into the rhombohedral phase ($R\bar{3}c$) at 145°C, remaining stable up to 900°C (5, 6). Initially it had been reported on the basis of X-ray diffraction (3, 4, 7, 8) that in $LaGaO_3$ (undoped or lightly doped with Sr and Mg) the symmetry remains orthorhombic, whereas heavier doping leads to cubic symmetry. However, a more recent high-resolution neutron diffraction study (9) indicates that doping affects symmetry and structure in a more complex way than was initially suggested. Slater *et al.* (9) report that $La_{0.9}Sr_{0.1}Ga_{0.80}Mg_{0.20}O_{2.85}$ adopts monoclinic $I2/a$ rather than orthorhombic *Pnma* symmetry. The change of symmetry relates to the structural difference in terms of the way the Ga(Mg)–O octahedra are tilted from their ideal positions in cubic perovskite according to Glazer's 23 tilt systems (10). The orthorhombic *Pnma* symmetry is a result of the octahedral tilts which can be described as $a^+b^-b^-$ (or $a^+a^-a^-$), where a and b denote the amount of tilt in respective $\langle 100\rangle_c$ directions, and the plus and minus signs indicate whether the tilts are in the same or opposite sense in the neighboring octahedra. The monoclinic $I2/a$ symmetry is a result of $a^-b^-b^-$ tilts. Thus the main difference between the two structures lies in the sense of the $[100]_c$ tilt; the neighboring octahedra are tilted in the same sense for the structure with *Pnma* symmetry and opposite for $I2/a$ symmetry. For the rhombohedral $R\bar{3}c$ symmetry, the

[1] To whom correspondence should be addressed.

0022-4596/99 $30.00

corresponding tilt system is $a^-a^-a^-$. Thus the structures in the monoclinic and rhombohedral symmetry are also closely related, differing only in the relative amount of tilt, while the sense of the tilt is the same.

2. EXPERIMENTAL

Samples of La(Sr)Ga(Mg)O_3 were prepared from powders of La_2O_3 (99.99%), Ga_2O_3 (99.99%), $SrCO_3$ (99.99%), and $MgCO_3$ (99.99%) from Alpha Products. The powders were thoroughly mixed with acetone in an agate mortar, pelletized, and fired in an alumina crucible at 1300°C for 24 h. The powder X-ray patterns showed that the desired compounds were usually formed at this stage. Otherwise, the samples were reground and refired. The final sintering was at 1430°C for 24 h followed by furnace cooling.

The sample with the highest ionic conductivity having the composition $La_{0.8}Sr_{0.2}Ga_{0.85}Mg_{0.15}O_{2.825}$ (7) was chosen for the detailed structural study. The ambient temperature neutron powder diffraction pattern of $La_{0.8}Sr_{0.2}Ga_{0.85}Mg_{0.15}O_{2.825}$ was measured at the High Flux Beam Reactor at Brookhaven National Laboratory in the range $15° < 2\theta < 156°$ with 0.05^0 steps and a wavelength of 1.8857 Å. The structure was refined by the Rietveld method (11) using the program FullProf (12) and coherent neutron scattering factors (13): $b(\mathrm{La}) = 0.824$, $b(\mathrm{Sr}) = 0.702$, $b(\mathrm{Ga}) = 0.729$, $b(\mathrm{Mg}) = 0.538$, and $b(\mathrm{O}) = 0.581$ (fm). The profile parameters (scale factor, zero point correction, background terms, pseudo-Voigt peak shape width variation terms, and a low angle asymmetry correction) were refined together with the lattice parameters, atomic coordinates, and atomic displacement parameters. Because of the similar cation scattering lengths and the correlation between atomic displacement parameters and occupation number, the relative La/Sr occupation of the $(\frac{1}{2}, \frac{1}{2}, \frac{1}{2})$ site and the Ga/Mg occupation of the $(0, 0, 0)$ site were fixed at that corresponding to the nominal stoichiometry. The occupancy of the oxygen site was refined, but not simultaneously with the displacement parameters.

Electron diffraction and high-resolution images were obtained using a JEOL 2010 FEG and Philips CM12 electron microscopes. The samples for the electron microscope study were prepared by crushing the powder in butanol and allowing a drop of the resultant suspension to dry on a holey carbon film. Electron diffraction patterns at temperatures between 25 and 900°C were obtained using a Gatan double tilt heating holder. To ensure good thermal contact of the sample with the heating element of the holder, the

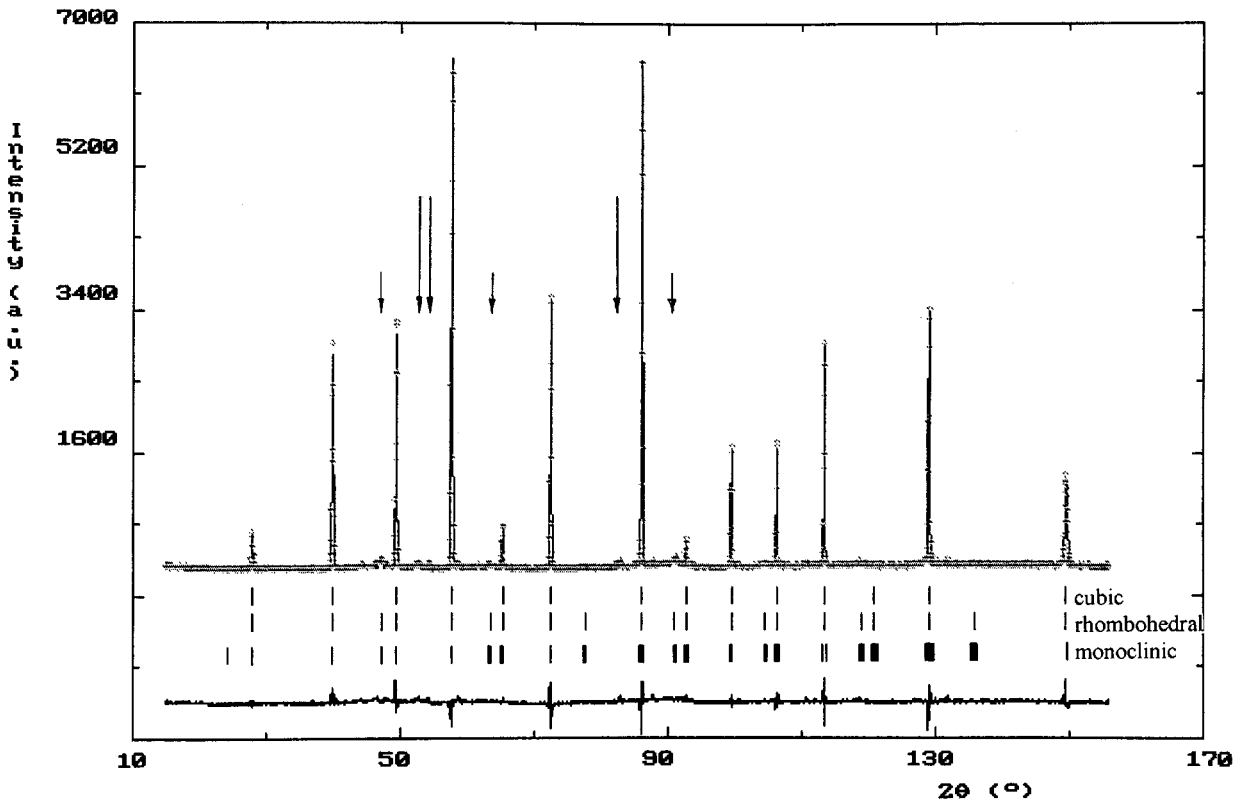

FIG. 1. The observed, calculated, and difference neutron powder diffraction profiles for $La_{0.8}Sr_{0.2}Ga_{0.85}Mg_{0.15}O_{2.825}$. The reflections identified with the shorter arrows could be indexed using the rhombohedral or monoclinic perovskite unit cell (6, 9), but those identified with the longer arrows could not be indexed. All were excluded for the final refinement of the structure.

transmission electron microscope (TEM) sample was prepared by dimpling and ion-milling a thin disc of pressed powder. A series of electron diffraction patterns from the same area of the crystal fragment were recorded at 50°C intervals while heating and cooling.

3. RESULTS

3.1. Powder Neutron Diffraction

The neutron diffraction pattern of $La_{0.8}Sr_{0.2}Ga_{0.85}Mg_{0.15}O_{2.825}$ was indexed to the cubic perovskite unit cell; i.e., no splitting of the parent perovskite reflections was detected. However, several very weak and broad peaks that could not be indexed on the cubic cell were also observed, as shown with arrows in Fig. 1. In view of the electron diffraction results, presented in the next sections, and because orthorhombic (*Pnma*), rhombohedral ($R\bar{3}c$), and monoclinic ($I2/a$) perovskite phases have been reported for pure and doped $LaGaO_3$, albeit at different temperatures (5, 6), we attempted to index and refine the pattern as a combination of the cubic phase and each of the lower symmetry phases using the reported coordinates as starting models. For the cubic phase, the ideal perovskite structure in space group $Pm\bar{3}m$ was used. Although the indexing of the weak peaks was equally better after the addition of the rhombohedral or monoclinic phase rather than orthorhombic phase, as seen in Fig. 1, even in these cases not all the peaks could be indexed and we obtained large R_{Bragg} factors. We considered the agreement too poor for a meaningful interpretation and refined only the cubic phase after excluding all the broad peaks from the spectrum. The crystallographic parameters of the refinement are given in Table 1, and the summary of the results for the isotropic and anisotropic models is given in Table 2. Figure 1 shows the observed, calculated, and difference powder patterns for the anisotropic model. The displacement parameters of the oxygen atoms are large and highly anisotropic, indicating that on average the oxygen atoms are displayed away from the ideal perovskite site at $(\frac{1}{2}, 0, 0)$ perpendicular to the Ga(Mg)–O bond. Such large displacement parameters suggest that tilts of the Ga(Mg)–O octahedra are present.

TABLE 1
Crystallographic Parameters for $La_{0.8}Sr_{0.2}Ga_{0.85}Mg_{0.15}O_{2.825}$

Empirical formula	$La_{0.8}Sr_{0.2}Ga_{0.85}Mg_{0.15}O_{2.825}$
Color and form	Ivory powder
Crystal system	Cubic
a (Å)	3.90889(4)
V (Å^3)	59.726
Z	1
Space group	$Pm\bar{3}m$ (No. 221)
T (K)	293
Radiation	Neutrons
λ (Å)	1.8857
Number of measurement points	2821
Number of reflections	14
Number of refined parameters	18

3.2. Electron Diffraction and Imaging

Electron diffraction shows that local structures with symmetry lower than cubic exist in $La_{0.8}Sr_{0.2}Ga_{0.85}Mg_{0.15}O_{2.825}$. Figure 2 shows the electron diffraction patterns obtained from a sample annealed for 3 weeks at 500°C. Qualitatively, the same patterns were found in the samples which were furnace cooled from 1430°C. Figure 2a shows the $[100]_c$ zone axis electron diffraction pattern. Weak and diffuse lines between the strong $(100)_c$ reflections are visible on the long exposure micrographs. The lines having nonuniform intensity are strongest in regions midway between the reflections. The relative intensity of these regions varied in different crystal fragments but an increase in intensity at the midpoint was generally observed. Figure 2b shows the $[110]_c$ zone electron diffraction pattern. The lines of diffuse scattering between the strong, $(100)_c$ reflections are visible in this projection as well. Apart from these features, there are also weak, but sharp reflections at $\mathbf{G} \pm \frac{1}{2}\langle 111\rangle_c^*$, as indicated with an arrow, which cannot be indexed on the primitive cubic unit cell.

High-resolution lattice images of thin crystal fragments in $[100]_c$ and $[110]_c$ projections are shown in Figs. 3 and 4,

TABLE 2
Structural Parameters and Refinement Agreement Indexes for Isotropic and Aniosotropic Thermal Displacement Parameters in $La_{0.8}Sr_{0.2}Ga_{0.85}Mg_{0.15}O_{2.825}$

Site	Atom	Position	Location	U (Å^2)	U_{11} (Å^2)	U_{22} (Å^2)	U_{33} (Å^2)	Occupancy
A	(0.8La + 0.2Sr)	1*a* ($m\bar{3}m$)	(0, 0, 0)	0.018	—	—	—	1.0
B	(0.85Ga + 0.15Mg)	1*b* ($m\bar{3}m$)	$(\frac{1}{1}, \frac{1}{2}, \frac{1}{2})$	0.012	—	—	—	1.0
O	O	3*d* (4/*mm*)	$(\frac{1}{2}, 0, 0)$	0.048	0.015	0.076	0.076	0.94

Note. For the isotropic model: $R_p = 0.084$, $R_{wp} = 0.116$, $R_{bragg} = 0.101$. For the anisotropic model: $R_p = 0.772$, $R_{wp} = 0.102$, $R_{bragg} = 0.0886$. $R_p = \sum|y_0 - y_c|/\sum|y_0|$. $R_{wp} = [\sum w(y_0 - y_c)^2/\sum wy_0^2]^{1/2}$. $R_{bragg} = \sum|I_0 - I_c|/\sum|I_0|$. $\chi^2 = 8.6$.

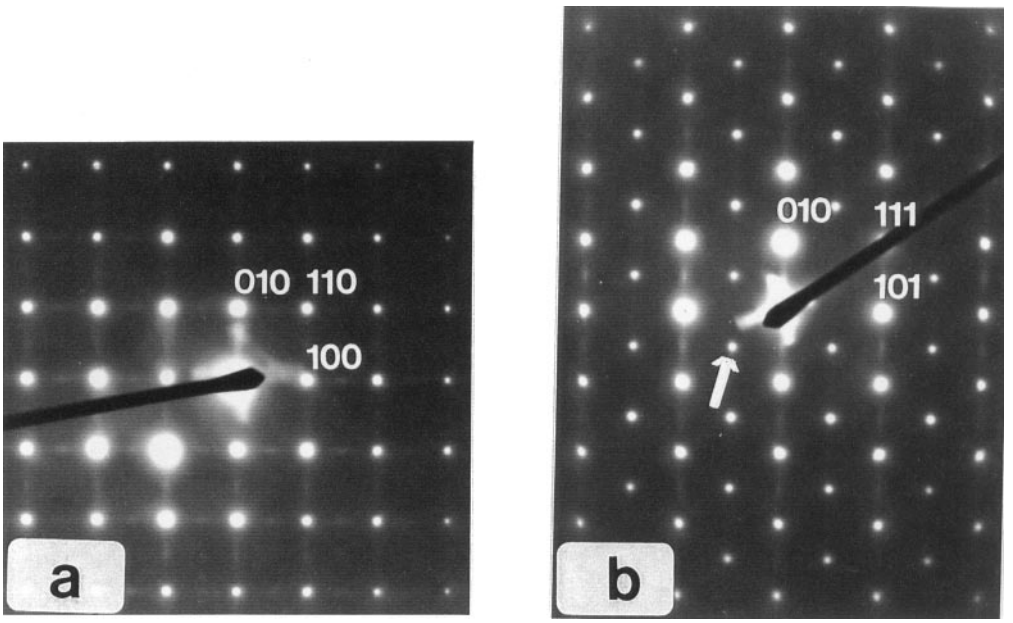

FIG. 2. (a) The $[100]_c$ zone electron diffraction pattern of $La_{0.8}Sr_{0.2}Ga_{0.85}Mg_{0.15}O_{2.825}$. Weak and diffuse streaks are visible between the $(100)_c$ reflections. The streaks have nonuniform intensity and are strongest in regions midway between the reflections. (b) The electron diffraction pattern in $[110]_c$ projection. The diffuse scattering between the strong $(100)_c$ reflections is visible. Also shown, as indicated with an arrow, are the weak and sharp reflections, which cannot be indexed on the primitive cubic unit cell.

respectively. The fragment imaged in the $[100]_c$ projection displays a contrast with the fourfold symmetry, in its thinnest parts, as expected. These contrast features are formed by the strong reflections in the diffraction pattern in Fig. 2a. The contrast corresponding to the weak, diffuse lines of scattering seen in Fig. 2a is not readily visible in the image. However, about 300 Å away from the edge of the crystal where the fragment is thicker, we may note additional contrast changes, i.e., rows of brighter and darker lines frequently spaced by $2a_c$ (the lines are indicated by arrows in Fig. 3). The contrast difference between the dark and bright lines is not large, and the lines are only 10–20 unit cells long, i.e., 40–80 Å. Although they tend to follow only one of the $\langle 100\rangle_c$ directions, the square pattern of the diffuse scattering in Fig. 2a is produced by superposition of the diffraction lines from domains where the ordering occurs in two perpendicular directions.

The image of the crystal lattice in the $[110]_c$ direction, shown in Fig. 4, clearly displays a domain structure. Two types of domains are present. For the first type, labeled B in Fig. 4, the contrast can be represented as a rectangular grid of dark (or white) points. For domains of the second type, which are typically 100–200 Å in diameter, labeled A, the contrast shows pseudo-hexagonal symmetry; i.e., the $\mathbf{G} \pm \frac{1}{2}\langle 111\rangle_c^*$ reflections are locally present. Complicated contrast is visible at the interfaces between the domains. Figure 5 shows a dark field image of a region in $[110]_c$ projection. The image was obtained using only one $\mathbf{G} \pm \frac{1}{2}$ $\langle 111\rangle_c^*$ type reflection. Only the regions which contribute to this particular reflection are imaged with lighter contrast. As seen from Fig. 5 such regions have a diameter of less than 200 Å.

3.3. *High-Temperature Electron Diffraction*

Figure 6a shows the initial diffraction pattern from a fragment oriented in the $[110]_c$ projection. It is convenient to relate this pattern to that in Fig. 2b. The weak diffuse streaking between the $(100)_c$ reflections is visible in both. However, the weak sharp reflections at $\mathbf{G} \pm \frac{1}{2}$ $\langle 111\rangle_c^*$, marked with an arrow in Fig. 2b, are not sharp on the diffraction pattern in Fig. 6a. Instead, these reflections have the appearance of crosses and the diffuse streaking also extends between the crosslike reflections. The first marked change upon heating of this crystal fragment was recorded at 650°C, when the crosslike reflections become diffuse spots, as shown in Fig. 6b. At 700°C they become sharp spots (Fig. 6c) and remain as such up to 900°C.

The lines of diffuse intensity between the $(100)_c$ reflections also change with heating. In the initial electron diffraction pattern, shown in Fig. 6a, the streaks of diffuse scattering are present and have markedly stronger intensity midway between the cubic reflections. After heating to approximately 500°C, the streaks almost completely disappear while the middle region retains its intensity, as visible in Fig. 6b and

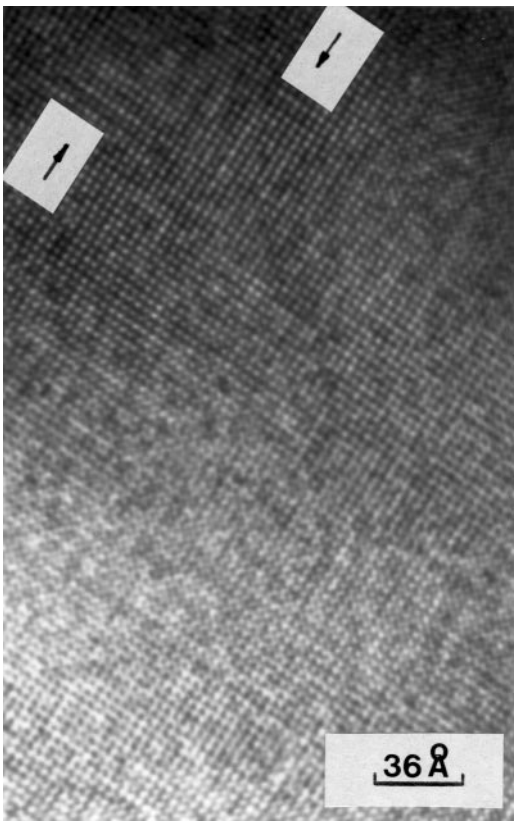

FIG. 3. The high-resolution lattice image in $[100]_c$ projection. The arrows indicate weak contrast features in the form of rows of brighter and darker lines spaced by a_c and 10–20 unit cells long (40–80 Å) in the thicker parts of the fragment.

6c. After heating to 900°C the intensity of these broad, diffuse reflections decreases but they remain visible. After rapid cooling to room temperature, all the diffuse streaking reappears, as seen in Fig. 6d.

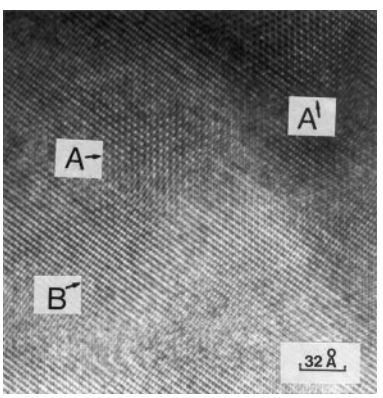

FIG. 4. The high-resolution lattice image in $[110]_c$ projection. In regions labeled A, the contrast corresponds to cubic perovskite, whereas those labeled B correspond to a lower symmetry perovskite. The latter domains are approximately 100–200 Å in diameter.

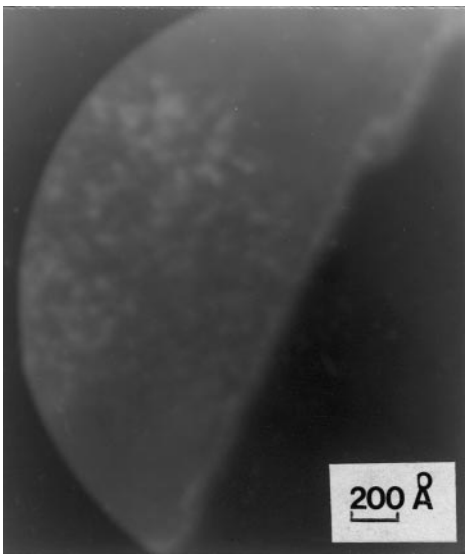

FIG. 5. Dark field image in $[110]_c$ projection obtained using the $\mathbf{G} \pm \frac{1}{2}\langle 111\rangle_p^*$ reflection indicated with an arrow in Fig. 2b. The image indicates that a superstructure is formed in approximately 200 Å domains, i.e., the regions imaged with bright contrast.

4. DISCUSSION

4.1. Powder Neutron Diffraction

The refinement of the powder neutron diffraction pattern resulted in highly anisotropic, large thermal displacement parameters for the oxygen atoms, indicating that the thermal motion is accompanied by rotation of the Ga(Mg)–O octahedra resulting in the bending of the Ga(Mg)–O–Ga(Mg) bonds. The average amount of the bending can be estimated from the thermal displacement parameters of the oxygen atoms as approximately 0.3 Å, which corresponds to a Ga(Mg)–O–Ga(Mg) angle of $\sim 162.5°$. The high anisotropy of the thermal displacement parameters is hardly surprising considering that most of the weak, broad superstructure reflections that have been omitted in the refinement could be indexed with rhombohedral or monoclinic cells where the Ga(Mg)–O octahedra are tilted away from the cubic positions. One may notice from Fig. 1 that in the absence of a detectable splitting of the parent cubic reflections, our low-resolution neutron diffraction data do not permit distinction between the rhombohedral and monoclinic space groups on the basis of the positions of the weak reflections alone. The origin of the broad reflections, indicated by the longer arrows in Fig. 1, which could not be indexed with the above cells, is not clear. They might originate from the regions of the planar ordering of the oxygen vacancies but more investigation would be necessary to establish this with more certainty.

From the electron diffraction patterns, $La_{0.8}Sr_{0.2}Ga_{0.85}Mg_{0.15}O_{2.825}$, although cubic on average, is composed of

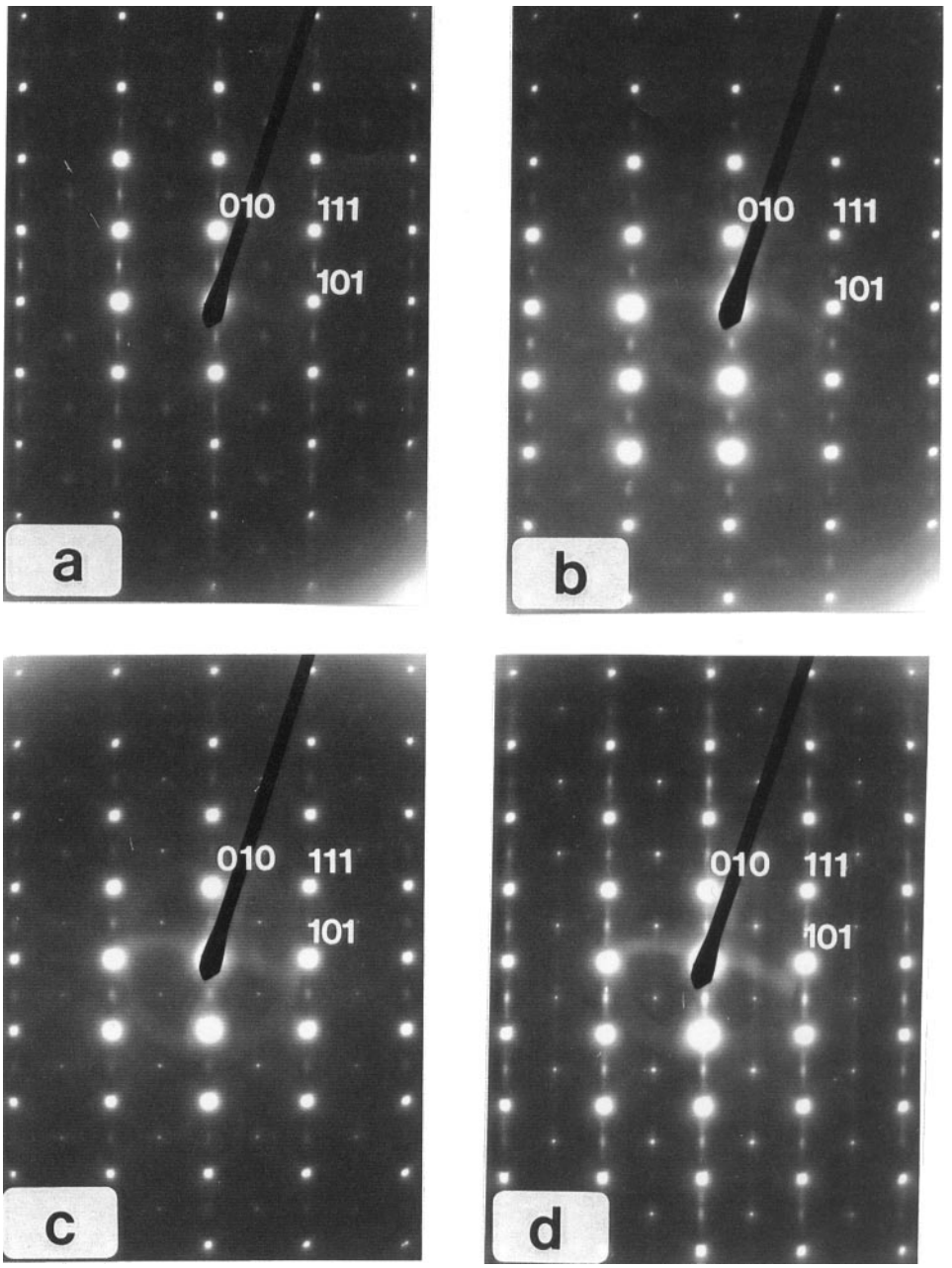

FIG. 6. Thermal evolution of the $[110]_c$ zone diffraction pattern. The sharp reflections, indicated with an arrow in Fig. 2, are diffuse in (a) and (b), indicating that the domains of the octahedral-tilt perovskite phase are initially small. These reflections became sharp after heating to approximately 700°C and remain sharp both during further heating and after cooling to room temperature (d), suggesting that coarsening of these regions had occurred. The streaks of diffuse scattering disappear during heating; they are not visible at 650°C, but reappear after cooling to room temperature.

small, randomly oriented regions. The size of these regions, visible in the dark field electron images, is about 200 Å in diameter and comparable with the coherent length of scattering of X rays or neutrons, thus causing the substantial broadening of the weak reflections observed on the powder neutron diffraction pattern.

4.2. Electron Diffraction and Imaging

Electron diffraction and imaging support the conclusion of randomly oriented regions with lower than cubic symmetry embedded in the cubic matrix. However, unambiguous assignment of the symmetry, and thus the perovskite tilt

system on the basis of the electron diffraction, is not possible. We simulated the dynamical selected area electron diffraction patterns expected for all the perovskite tilt systems using the coordinates from Woodward (14) and the EMS package (15). After allowing for the violation of the extinction conditions caused by the glide planes and screw axis, which occurs in the dynamical electron diffraction due to bending of the crystal fragment from the exact zone orientation, as described by Gjonnes and Moodie (16) and tabulated by Tanaka *et al.* (17), we concluded that the observed selected area diffraction patterns will be identical with the calculated ones for six space groups, i.e., six tilt systems: $F-1$ ($a^-b^-c^-$ tilt system), $I2/a$ ($a^-b^-b^-$), $R\bar{3}c$ ($a^-a^-a^-$), $I2/m$ ($a^0b^-c^-$), $Imma$ ($a^0b^-b^-$), and $I4/mcm$ ($a^0a^0c^-$). Convergent beam diffraction will narrow the above possibilities when the Gjonnes–Moodie lines in certain diffraction discs of appropriately oriented diffraction patterns are observed. More experiments are planned to systematically study the convergent beam diffraction in the above systems to establish a frame of reference for $La_{0.8}Sr_{0.2}Ga_{0.85}Mg_{0.15}O_{2.825}$. With the presently available information we can only speculate that the small regions of lower symmetry observed in our samples are most likely to have $I2/a$ or $R\bar{3}c$ symmetry since those have already been observed in the system. In what follows we will refer to the structure of these regions as octahedral-tilt perovskite.

Due to the strong scattering of the electrons, the weak streaks between the $(100)_c$ reflections could be recorded on the electron diffraction patterns (Fig. 2). Since the streaking is essentially one-dimensional, the square pattern in Fig. 2a is produced by superposition of streaking in two perpendicular directions. It cannot be explained by thermal diffuse scattering, i.e., the excitation of low energy phonon modes of the perovskite rigid-octahedra framework, as calculated by Giddy *et al.* [19], i.e., cannot be associated with rotations of the octahedra. Instead, the diffuse streaking implies the existence of correlated sheets of atoms perpendicular to $\langle 100\rangle_c$. The thermal behavior of the streaking indicates that it is associated with a fast moving ion such as oxygen in $La_{0.8}Sr_{0.2}Ga_{0.85}Mg_{0.15}O_{2.825}$; planar ordering of the oxygen vacancies is thus the most probable cause of the streaking. The increase in the intensity of the streaking midway between the cubic reflections indicates that, although the vacancy planes are spaced randomly, there are sizable regions in which the distance between them is $2a_c$. In our study of Sr- and Mg-doped $LaGaO_3$ single crystals, we observed diffuse and elongated reflections in the same reciprocal space region, and we attributed them to a structure with tetragonal unit cell $a_c \times 2a_c \times a_c$, where a_c is the lattice parameter of the cubic perovskite (20). We proposed structural models of oxygen vacancy ordering into planes, corresponding to the observed unit cell, and concluded that the most likely arrangement is that of the brownmillerite-like structure with vacancy planes spaced by $2a_c$. Similar vacancy ordering into brownmillerite-like domains has also been observed for other heavily doped perovskites by Adler *et al.* (1).

4.3. High-Temperature Electron Diffraction

The electron diffraction patterns indicate a complex microstructure in $La_{0.8}Sr_{0.2}Ga_{0.85}Mg_{0.15}O_{2.825}$. Figure 7 illustrates possible changes in microstructure with temperature. At room temperature, the microstructure consists of small domains of randomly oriented octahedral tilt perovskite embedded in a cubic perovskite matrix, as indicated by the oval shapes in Fig. 7a. Also embedded are small domains, indicated with rectangles, in which the vacancy planes are ordered and the average distance between them is $2a_c$. The structure of these regions is likely to be brownmillerite-like. In the cubic matrix, between the octahedral-tilt perovskite and brownmillerite-like domains, there are also randomly spaced planar clusters of oxygen vacancies (labeled disordered vacancy planes), which are, at most, only several nanometers in diameter. Both the ordered and disordered oxygen vacancy planes are parallel to any of the three $\{100\}_c$ planes, thus forming a twinned microstructure. The randomly spaced planar vacancy clusters are stable up to approximately 500°C, above which they disorder completely into the cubic matrix, as shown in Fig. 7b. The brownmillerite-like domains are more stable upon heating, decreasing in number and/or in size, but persisting even at 900°C (Fig. 7c). The difference between the brownmillerite-like domains and the planar clusters lies in the degree of order in the separation distance between the oxygen vacancy planes. In the former, the planes are spaced on average by $2a_c$ while their spacing is random in the latter, making the disordered clusters apparently less stable than the more ordered domains. The reappearance of streaking after rapid cooling from 900°C to room temperature, shown in Fig. 7d, strongly supports the notion that the superstructure is formed by rapid ordering of a highly mobile ion, such as oxygen, into planes.

The order–disorder transition, i.e., formation and disappearance of the planar vacancy clusters and the gradual disordering of the brownmillerite-like regions, correlates well with the decrease in the conduction activation energy observed above 500°C (4, 7). It had already been postulated by Feng and Goodenough (4) that the change of the activation energy could be caused by an order–disorder transition of a short-range oxygen vacancy clustering. The present high-temperature electron diffraction study provides further evidence for such a transition.

Unlike the regions with planar oxygen vacancy ordering, the octahedral-tilt perovskite regions, once formed in large enough domains to result in sharp reflections, near 700°C as seen in Fig. 7c, do not disorder nor detectably decrease in size upon heating and can be readily quenched to room temperature. Consequently, we anticipate that these regions

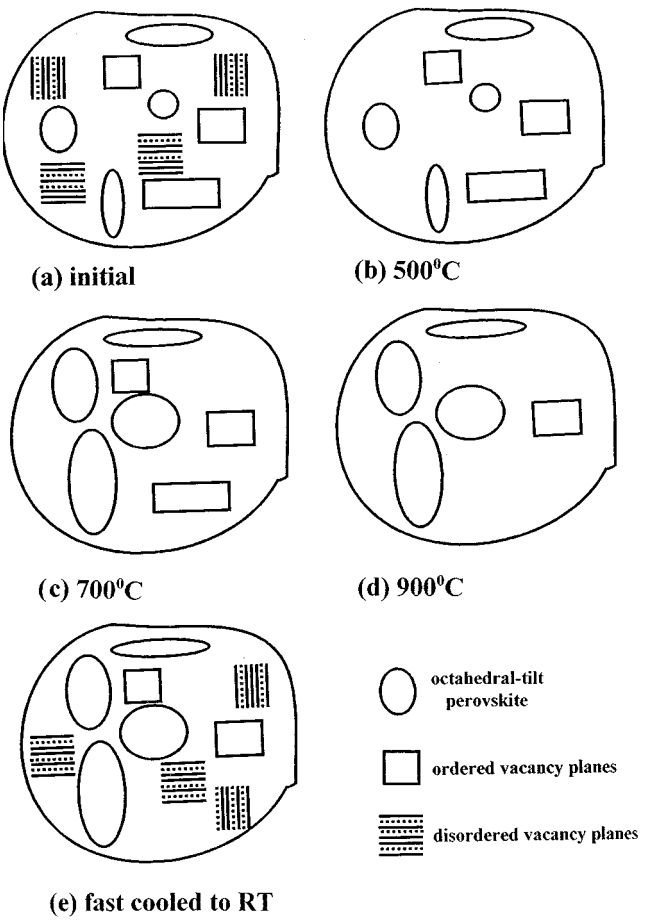

FIG. 7. Changes in the microstructure of $La_{0.8}Sr_{0.2}Ga_{0.85}Mg_{0.15}O_{2.825}$ during heating.

play a small role in the decrease of the conduction activation energy at high temperatures. The formation, symmetry, and size of these noncubic regions may be quite sensitive to local variations in composition since the monoclinic symmetry has been reported for a composition close to $La_{0.8}Sr_{0.2}Ga_{0.85}Mg_{0.15}O_{2.82}$ (9). However, we anticipate that the lowering of symmetry from cubic to rhombohedral, monoclinic, or other by means of octahedral tilt, as opposed to the cooperative ordering of oxygen vacancies, should not affect the change in the conduction activation energy in an equally profound manner.

5. CONCLUSIONS

Electron diffraction at ambient and elevated temperatures was used to show that the microstructure of $La_{0.8}Sr_{0.2}Ga_{0.85}Mg_{0.15}O_{2.825}$ has lower local symmetry than the average cubic found by neutron or X-ray diffraction. Two types of local microstructures are present. The first originates from the typical perovskite cooperative tilting of Ga(Mg)–O octahedra and is formed at high temperatures but remains stable on quenching. The second, related to ordering of the oxygen vacancies into planes, can be destroyed by heating and rapidly restored after cooling, and correlates with the decrease in the conduction activation energy.

ACKNOWLEDGMENTS

We thank Tom Vogt for measuring the neutron diffraction spectra. We also thank Ontario Hydro for a loan of the Gatan heating holder. The financial support through a collaborative grant from the Natural Sciences and Engineering Research Council of Canada is also gratefully acknowledged.

REFERENCES

1. S. Adler, S. Russek, J. Reimer, M. Fendorf, A. Stacy, Q. Huang, A. Santoro, J. Lynn, J. Baltisberg, and U. Werner, *Solid State Ionics* **68,** 193 (1994).
2. J. M. González-Calbet, M. Parras, M. Vallet-Regí, and J. C. Grenier, *J. Solid State Chem.* **92,** 110 (1991).
3. T. Ishihara, H. Matsuda, and Y. Takida, *J. Am. Chem. Soc.* **116,** 3801 (1994).
4. M. Feng and J. B. Goodenough, *Eur. J. Solid State Inorg. Chem.* **31,** 663 (1994).
5. Y. Wang, X. Liu, G.-D. Yao, R. C. Liebermann, and M. Dudley, *Mat. Sci. Eng.* **A132,** 13 (1991).
6. W. Marti, P. Fischer, F. Altorfer, H. J. Scheel, and M. Tadin, *J. Phys. Condens. Matter* **6,** 127 (1994).
7. P. Huang and A. Petric, *J. Electrochem. Soc.* **143,** 1644 (1996).
8. J. Drennan, V. Zelizko, D. Hay, F. F. Ciacchi, S. Rajendran, and S. P. S. Badwal, *J. Mater. Chem.* **7,** 79 (1997).
9. P. R. Slater, J. T. S. Irvine, T. Ishihara, and Y. Takita, *Solid State Ionics* **107,** 319 (1998).
10. A. M. Glazer, *Acta Crystallogr. Sect. A* **31,** 756 (1975).
11. H. M. Rietveld, *J. Appl. Crystallogr.* **2,** 65 (1969).
12. R. Rodriguez-Carvajal, Program FullProf, version 2.4.2. Dec. 1992.
13. "International Tables for Crystallograhy," Vol. 3, p. 384, Table 4.4.4.1. Kluwer Academic, Dordrecht/Norwell, MA, 1992.
14. P. M. Woodward, *Acta Crystallogr. Sect. B* **53,** 32 (1997).
15. P. Stadelmann, Electron microscopy image simulation on line, available at http://cimewww.epfl.ch.CIOL.ems.html.
16. J. Gjonnes and A. F. Moodie, *Acta Crystallogr.* **19,** 65 (1965).
17. M. Tanaka, H. Sekii, and T. Nagasawa, *Acta Crystallogr. Sect. A* **39,** 825 (1983).
18. A. P. Giddy, M. T. Dove, G. S. Powley, and V. Heine, *Acta Crystallogr. Sect. A.* **49,** 697 (1993).
19. A. Skowron, A. Petric, and H. Dąbkowska, submitted for publication.